Near-Surface Microearthquakes at The Geysers Geothermal Field, California

James T. Rutledge
Nambe Geophysical, Inc., Route 1 Box 104F, Santa Fe, NM 87501
email: jrutledge@lanl.gov, fax: 505-667-8487

Mitchel A. Stark
Calpine Corporation, 10350 Socrates Mine Road, Middletown, CA 95461

Thomas D. Fairbanks
Nambe Geophysical, Inc., Route 1 Box 104F, Santa Fe, NM 87501

Timothy D. Anderson
Sonoma County Water Agency, P.O. Box 11628, Santa Rosa, CA 95406

Submitted to Pure and Applied Geophysics

April, 2000

LAUR# 00-1554

Keywords: Induced seismicity, microearthquake, wellbore deformation, geothermal

Abstract

A 150-m length, 6-level, 3-component, vertical geophone array was cemented into the 67- to 219-m depth interval (220 to 720 ft) of Unocal's well GDCF 63-29 during a plug and abandonment operation on April 7, 1998. Casing deformation has been observed in wells of the study area including the GDCF 63-29 well. An objective of the study was to determine if shallow deformation at The Geysers is manifested seismically. Near-surface microearthquake activity was monitored for a period of one year; during the latter 4 months, monitoring was supplemented with four surface stations to help constrain locations of shallow seismicity. Event locations occurring within about 750 m of the array bottom have been determined for the 10-week period January 6 to March 16, 1999. These events are distinct from surface-monitored seismicity at The Geysers in that they occur predominantly above the producing reservoir, at depths ranging from about 220 to 1000 m (600 to -180 m elevation). The shallow events tend to be episodic, with relatively quiescent periods of up to three weeks occurring between swarms. Event locations show a northeast-striking trend, similar to seismicity trends mapped deeper in the reservoir, and parallel to the strike of a major surface lineaments observed over the productive field. However, clear fault or fracture planes are not resolved from the hypocenters. Composite fault-plane solutions suggest oblique reverse faulting in the overburden. The shallowest seismicity terminates near the base of a serpentine unit, a contact which is the locus of most of the well casing deformations logged in the area, suggesting that reservoir contraction is accommodated along numerous discrete faults below the serpentine, but as continuous plastic deformation in the serpentine. It is hypothesized that the resulting strain discontinuity at the base of the serpentine explains the prevalence of wellbore deformation there. The shallow, above-reservoir microseismicity is strongly correlated in time with the injection and the deeper injection-induced seismic activity occurring in the reservoir

immediately below. This suggests that deep injection-induced events trigger shallower events, by a remote triggering mechanism which has been observed at a larger scale at The Geysers and elsewhere.

Introduction

Since fractures usually dominate the contribution to permeability in geothermal reservoirs, the ability to map them at large distance from boreholes has direct applications to reservoir development and management. It is well known that the gross flow paths affected by hydraulic fracturing can be mapped using the microearthquakes induced during the treatment. Barton et al., (1995) have shown correlations of high permeability along fractures that are oriented such that resolved shear stress is high. If this is generally true, it would imply that any reservoir stress changes that even weakly promote failure on critically stressed fractures could result in seismicity that reveals important or potentially important reservoir flow paths. Stress changes can also be induced outside the reservoir, where no pore-fluid content changes need occur, due to reservoir volume changes accompanying pressure and temperature drawdown (e.g., Segall, 1989; Segall and Fitzgerald, 1998). Microearthquakes induced above the reservoir could be used for monitoring and characterizing deformation in the overburden.

Seismic station coverage of The Geysers region was greatly enhanced in the mid-1970's by the U.S. Geological Survey, leading to early recognition and characterization of production-induced seismicity (Marks et al., 1978; Majer and McEvilly, 1979; Denlinger and Bufe, 1982; Eberhart-Phillips and Oppenheimer, 1984; Oppenheimer, 1986). Hypocentral resolution was improved when steamfield operators, such as the Unocal-NEC-Thermal partnership (U-N-T), set up field wide array coverage (Stark, 1990), and was further refined with denser arrays covering specific areas within the field (Kirkpatrick et al, 1995; Romero et al, 1995; Julian et al, 1993).

Detection thresholds for these arrays ranged as low as M = –1. Data collected on the high-resolution arrays have been used to help understand the reservoir by: 1) associating hypocenter patterns with fluid movement (Stark, 1990; Kirkpatrick et al., 1995), 2) associating seismic velocity anomalies with specific lithologies, reservoir processes, and saturation levels (Romero et al., 1995; Kirkpatrick et al., 1997), and 3) inferring reservoir fracture behavior or mechanics by associating extraction/injection operations with seismic source characteristics (Julian et al., 1993; Kirkpatrick et al., 1995; Ross et al., 1999).

Downhole seismic receivers deployed as deep as 712 m (~280 m above the reservoir) at The Geysers lowered the threshold of detection to M = –3, or 2 to 3 magnitude units below the limits of surface monitoring (Albright et al., 1998). Placing seismic sensors downhole also results in a concomitant increase in event detection rate for a given volume of rock and, in general, greatly improves the resolution of mapping active reservoir fractures or faults (e.g., Phillips et al., 1997; Rutledge et al., 1998a; Gaucher et al., 1998; Rutledge et al., 1998b; Phillips, 2000).

In this paper, we present microearthquake mapping results from monitoring with a borehole geophone array that was cemented within the upper 220 m (720 ft) of Unocal's well GDCF 63-29 in the southeast Geysers (Figures 1 and 2). Approximately 0.5 m of subsidence has occurred in the immediate study area between 1977 and 1996 and has been attributed to deeper, production induced reservoir contraction (Mossop and Segall, 1997). Near-surface strain has also been observed as casing deformation in this area of the field, occurring over short depth intervals where the wells intersect the upper and lower contacts of a serpentine unit dipping to the northeast (Figure 3). In fact, GDCF 63-29 was plugged and abandoned because of the severity of wellbore collapse concentrated at the base of the serpentine, at 244 m (800 ft) depth. Monitoring shallow microseismicity could potentially provide answers to questions regarding the nature of

deformation affecting borehole integrity, such as: Is the deformation episodic? Are the collapse zones associated with shallow fault zones intersecting the wellbores? and Can intersection with active, shallow faults or deformation zones be avoided?

Data

The downhole array installed in GDCF 63-29 is 152 m (500 ft) long with six 3-component sondes spaced at 30 m (100 ft) intervals (Figure 2). Deployment took place on April 7, 1998 during plug and abandonment of the well; all but the middle sondes S3 and S4 continued to operate with at least one functional geophone channel after one year of continuous monitoring. The temperature at the bottom of the array is 146° C. Details of the deployment and array specifications are given in Albright et al. (1998).

The array's short length and placement about 750 m above the reservoir makes it best suited for detecting and locating small microearthquakes associated with near-surface deformation. The downhole array was supplemented with four 3-component, surface-deployed geophones surrounding the GDCF 63-29 monitor well in late 1998 and early 1999 (Figure 2). It is possible to uniquely determine source locations from a single vertical array if good azimuthal data can be obtained from the horizontal component first-arrival particle-motion trajectories (e.g., Rutledge et al., 1998a). All events detected on the borehole array occur beneath the bottom sonde, most with steep travel paths from source to receiver. This results in low signal-to-noise-ratio first arrivals on the horizontal components and hence, unreliable azimuthal data. Adding the surface stations allowed locations to be determined using only the P and S arrival-time data.

The six downhole receiver levels and three of the surface stations were equipped with OYO GS-20DM geophones (28 Hz downhole, 14 Hz at surface); the fourth surface station was a Mark Products 1-Hz, L4-3C geophone. Using existing telemetry lines in the field, surface station output

were sent directly to the same PC-based data acquisition system used for the downhole receivers. Data were sampled at a 0.2 msec interval per channel. Downhole signal bandwidth above noise extends from about 20 to 400 Hz.

All data collected from April 7, 1998 to March 16, 1999, have been screened to select only those events occurring within about 750 m of the array (based on the criteria S-P arrival time difference ≤ 150 msec at the deepest station (S6, Figure 2)). Details of event occurrence over an 88-day period in 1998 shows that the shallowest seismicity is episodic. Within about 500 m of the array, relatively quiescent periods of up to three weeks are observed between swarms of events (Figure 4). In this paper we present the locations of near-array events detected on the borehole receivers and at least three of our local surface stations for the period January 6 to March 16, 1999. A total of 535 events were detected within ~750 m of the deepest station for this 70-day period. An example of a high-quality, near-array event recorded on downhole sonde S5 is shown in Figure 5.

The downhole array also detects events occurring field wide, in common with the U-N-T surface array. However, the shallow, local events analyzed are unique to our downhole array because they are generally too small for common detection over the wider station spacing (≥ 1 km) of the U-N-T surface array.

Determining Source Locations

Seismic velocities were determined using 1) surface calibration shots, 2) observed travel time differences across the downhole array, and 3) a velocity grid search to find the best fit between observed and computed arrival times. P- and S-wave velocities (Vp and Vs, respectively) were first computed for a shallow serpentine unit from the surface to 244 m depth using the surface shots and microearthquakes with travel paths within 10° of the vertical array. With these shallow

velocities fixed, we then did a grid search for an underlying half-space's Vp and Vs values that minimized the difference between observed and computed arrival times in a least-squares sense. The grid search resolved Vs very well but could not constrain Vp. Our top-layer Vp value is within 2% of the velocity model of Kirkpatrick et al. (1997) for the upper kilometer of the southeast Geysers. Therefore, we kept Vp constant across the 244 m serpentine contact. The final velocity model is summarized in Table 1. Trial runs to compare the resultant source locations and residual misfits with the model interface at 244 m oriented horizontal or dipping 30° to the NE (as in Figure 3) showed little difference. The results shown are for the flat-layered model.

Of the 535 events, 304 with at least six arrival times identified over the full length of the downhole array, and three or more arrival time picks on the surface stations, were considered for mapping. 297 location solutions converged, of which 248 had root-mean-square travel-time residuals less than 5 msec and location errors less than ±60 m (Figure 6). P and S station corrections were applied based on the median travel time residuals determined from two initial location runs. Arrival-time errors were estimated from the standard deviations of the travel-time residuals, and ranged from 2 to 5 msec. The location error ellipses displayed in Figures 6, 7 and 8 only reflect the arrival-time data errors, data distribution and array geometry; velocity model uncertainties are not considered. Median principle error axes for the 248 events displayed is ±24 m.

Microearthquake Maps

The map view (Figure 6) shows a gross northeast striking trend, similar to seismicity trends mapped deeper within the reservoir (e.g., Romero et al., 1995) and parallel to the strike of a major surface lineament observed over the productive field (Nielson and Nash, 1997). A depth view projecting the locations onto a plane orthogonal to the map trend is shown in Figure 7. Figure 8

shows a depth projection along the same profile direction as Figure 3. The shallowest steam entries in this area occur at about -180 m elevation. The events mapped are distinct from most surface-monitored seismicity in that they lie above the producing reservoir. Preliminary, downhole monitoring at this site indicated the shallow seismicity magnitudes ranged from about -3 to 0 (Albright et al., 1998). Two major clusters are identified in the strike-direction depth view (Figure 7). The shaded square-symbol cluster forms a low-angle feature dipping approximately 30° southeast. The same symbols are used in the map view to aid in visualizing the 3-dimensional distribution of hypocenters. The depth view looking along strike of the serpentine interface (Figure 8) shows that the shallowest seismicity terminates near the base of the serpentine, the boundary known to accommodate much of the near-surface strain, as manifest from the well casing deformations in the area (Figure 3).

Injection and near-surface seismicity

Seismicity and injection activity at the Geysers typically show strong temporal and spatial correlations (Stark, 1990; Beall et al., 1999). Figure 9 shows this to be true in this small study area of The Geysers, for both the overburden (that is, above the shallowest steam entries) and the deeper, reservoir microseismicity. Figure 10 shows the difference in depth distribution for our near-array events and the U-N-T surface-network-detected events for the same epicentral area. The shallow, near-array events are not energetic enough for common detection over the larger station spacing (≥ 1 km) of the U-N-T surface array, therefore, the overburden seismicity is a subset of the total downhole-detected event population unique to our local array. The gross rate change in overburden seismicity tracks right along with changes in the deeper, reservoir seismicity. Both cumulative-event count curves increase in slope within about 1 week of the increased injection rate, starting at about day 380 (Figure 9). We also looked for correlations

between production and the shallow seismicity, using the production wells shown in Figure 2. No clear temporal correlation between production and event rate was evident.

Focal Mechanisms

Composite fault-plane solutions were computed (Figure 11) for the square- and triangle-symbol hypocenter groups (Figures 6 and 7) using the computer program FPFIT (Reasenberg and Oppenheimer, 1985). Convergence to a single solution was achieved for both cases and both indicate a component of reverse faulting (triangle group predominantly so). The square-symbol group solution is better constrained and has fewer discrepant first-motion data.

Discussion

For depths between 1 and 5 km at The Geysers, inversion of focal mechanisms for stress tensors indicates a normal faulting stress regime that is transitional to strike-slip (i.e., the maximum horizontal stress is approximately equal to lithostatic load) (Oppenheimer, 1986). For the upper 1 km, focal mechanisms over large areas of the field include reverse faulting as well as normal and strike slip failures. As a result the stress regime is very poorly resolved at shallow depths. The stress regime could very well transition to reverse faulting at the near surface as the lithostatic load decreases. Oppenheimer (1986) also noted that the rugged topography at The Geysers could result in rapid lateral variations in the stress field and may in part explain the highly variable focal mechanisms observed at shallow depths over larger areas of the field. Reverse faulting at shallow depths will further be promoted as a result of reservoir contraction accompanying pressure and temperature drawdown (Segall and Fitzgerald, 1998).

The first motion data suggest a reverse faulting stress regime locally above the reservoir (< 750 m depth). However, the lack of clear planar distribution of the grouped hypocenters leaves no corroborative evidence that the nodal planes are reasonable and leaves in question whether the

compositing of first motion data is justified. The northeast striking nodal plane for the better-constrained, square-symbol-group solution (N37E) closely corresponds to the gross trends of seismicity seen in map view, and could indicate that failure predominantly occurs along similarly-oriented, steeply-dipping fractures (Figure 11). The difference in P-axes orientations between the two solutions would indicate that the focal mechanisms do not represent planes of maximum resolved shear and/or that the principle stress axes orientations in the overburden varies over short distances (~600 m).

Serpentinites are known to be mechanically weak, particularly at the temperatures encountered for this study (< 150° C) (Moore et al., 1997). The termination of seismicity near the base of the serpentine (Figure 8) and the concentration of wellbore deformation at that interface (Figure 3) suggest that strain transitions from brittle to more ductile deformation there. Volumetric contraction, accumulated on numerous discrete small faults below the serpentine, could be accommodated in the form of continuous plastic deformation in the overlying serpentine. This would create a strain discontinuity across the basal contact of the serpentine, subjecting the well casings to stress buildup and eventually failure. Repeated caliper logs from several wells of the area shows spotty patterns of deformation rates and magnitudes. The caliper logs are not oriented, so no direction or sense of motion is obtained from these periodic “strain” measurements. Oriented caliper logs might indicate if a uniform sense of motion occurs at inter-well scales and may provide insight into the kinematics of strain concentration and transition at the serpentine boundaries.

The short-term correlation of shallow seismicity with injection is impossible to explain in terms of pore pressure diffusion or local reservoir volume reduction. Rather, the shallow seismicity may be triggered by the more energetic reservoir seismicity via dynamic (e.g. Stark and

Davis, 1996) and/or quasi-static stress transfer.

Conclusions

Our ability to detect and locate the shallow seismicity can be attributed to placing geophones downhole and deploying surface stations close enough to enable detection of these low-magnitude events on multiple sensors. Composite fault-plane solutions suggest oblique reverse faulting above the reservoir. Seismicity is nearly absent above the base of a serpentine unit. This lithologic contact is known to accommodate much of the near-surface strain, as evident from the well casing deformations in the area. The concentration of casing deformation at the contact may be due to strain discontinuity between a plastic deformation regime in the serpentine and a brittle deformation regime below. The shallow, above-reservoir microseismicity is strongly correlated in time with the reservoir injection and reservoir injection-induced seismic activity occurring just below. This correlation is best explained as a small-scale example of remote triggering, as previously observed on a larger scale at The Geysers and elsewhere.

Acknowledgments

Unocal Corporation and Calpine Corporation granted access to the well and field facilities and provided personnel to assist in the work. We thank Steve Whitt and Mike Woodall for their assistance in the field work. Baljit Singh, with assistance from Jim Thomson, planned and supervised the well abandonment and array installation operations. Joe Beall provided valuable discussions on data analysis and interpretation. This work was funded by the U.S. Department of Energy’s Office of Geothermal Technologies.

References

Albright, J. N., Rutledge, J.T., Fairbanks, T.D., Thomson, J.C., and Stevenson, M.A. (1998), Vertical Arrays for Fracture Mapping in Geothermal Systems, Geotherm. Resources Counc. Trans., 22, 459-463.

Barton, C.A., Zoback, M.D. and Moos, D. (1995), Fluid Flow Along Potentially Active Faults in Crystalline Rock, Geology, 23, 683-686.

Beall, J.J., Stark, M.A., Smith, J.L., and Kirkpatrick, A. (1999), Microearthquakes in the Southeast Geysers Before and After SEGEP Injection, Geotherm. Resources Counc. Trans., 23, 253-257.

Denlinger, R.P. and Bufe, C.G. (1982), Reservoir Conditions Related to Induced Seismicity at The Geysers Steam Reservoir, Northern California, Bull. Seism. Soc. Am., 72 1317-1327.

Eberhart-Phillips, D. and Oppenheimer, D.H. (1984), Induced Seismicity in The Geysers Geothermal Area, California, J. Geophys. Res., 89, 1191-1207.

Gaucher, E., Cornet, F.H., Bernard, P. (1998), Induced Seismicity Analysis for Structure Identification and Stress Field Determination, SPE paper 47324, Soc. Petro. Eng. / Int. Soc. Rock Mech., Proc. Eurock 98, Trondheim, Norway.

Julian, B.R., Miller, A.D., and Foulger, G.R. (1993), Non-Shear Focal Mechanisms of Earthquakes at The Geysers, California, and Hengill, Iceland, Geothermal Areas, Geotherm. Resources Counc. Trans., 17, 123-128.

Kirkpatrick, A., Peterson, J.E. and Majer, E.L. (1995), Microearthquake Monitoring at the Southeast Geysers Using a High-Resolution Digital Array, Proc. 20th Workshop on Geotherm. Reservoir Engineering, Stanford University, Stanford, California, 79-89.

Kirkpatrick, A., Peterson, J.E., and Majer, E.L. (1997), Three-Dimensional Compressional- and Shear-Wave Seismic Velocity Models for the Southeast Geysers Geothermal Field, California, Proc. 22nd Workshop on Geotherm. Reservoir Engineering, Stanford University, Stanford, California, 399-410.

Majer, E.L., and McEvilly, T.V. (1979), Seismological Investigations at The Geysers Geothermal Field, Geophysics, 44, 246-269.

Marks, S.M., Ludwin, R.S., Louis, K.B., and Bufe, C.G. (1978), Seismic Monitoring at The Geysers Geothermal Field, California, U.S. Geol. Surv., Open-File Rept. 78-798.

Moore, D.E., Lockner, D.A., Ma, S., Summers, R., and Byerlee, J.D. (1997), Strengths of Serpentinite Gouges at Elevated Temperatures, J. Geophys. Res., 102, 14787-14801.

Mossop, A., and Segall, P. (1997), Subsidence at The Geysers Geothermal Field, N. California from Comparison of GPS and Leveling Surveys, Geophys. Res. Lett., 24, 1839-1842.

Nielson, D.L., and Nash, G.D. (1997), Structural Fabric of The Geysers, Geotherm. Resources Counc. Trans., 21, 643-649.

Oppenheimer, D.H. (1986), Extensional Tectonics at The Geysers Geothermal Area, California, J. Geophys. Res., 91, 11463-11476.

Phillips, W.S., House L.S., and Fehler, M.C. (1997), Detailed Joint Structure in a Geothermal Reservoir from Studies of Induced Microearthquake Clusters, J. Geophys. Res., 102, 11745-11763.

Phillips, W.S. (2000), Precise Microearthquake Locations and Fluid Flow in the Geothermal Reservoir at Soultz-sous-Forets, France, Bull. Seism. Soc. Am., 90, 212-228.

Reasenberg, P. and Oppenheimer, D. (1985), FPFIT, FPPLOT and FPPAGE: Fortran Computer Programs for Calculating and Displaying Earthquake Fault-Plane Solutions, U.S. Geological Survey, Open-File Report 85-0739.

Romero Jr., A.E., McEvilly, T.V., Majer, E.L., Vasco, D. (1995), Characterization of the Geothermal System Beneath the Northwest Geysers Steam Field, California, from Seismicity and Velocity Patterns, Geothermics, 24, 471-487.

Ross, A., Foulger, G.R., and Julian, B.R. (1999), Source Processes of Industrially-Induced Earthquakes at The Geysers Geothermal Area, California, Geophysics, 64, 1877-1889.

Rutledge, J.T., Phillips, W.S., and Schuessler, B.K. (1998a), Reservoir Characterization Using Oil-Production Induced Microseismicity, Clinton County, Kentucky, Tectonophysics, 289, 129-152.

Rutledge, J.T., Phillips, W. S., House, L.S., Zinno, R.J. (1998b), Microseismic Mapping of a Cotton Valley Hydraulic Fracture Using Decimated Downhole Arrays, 68th Ann. Mtg., Soc. of Explor. Geophys., Expanded Abstracts, 338-341.

Segall, P. (1989), Earthquakes Triggered by Fluid Extraction. Geology, 17, 942-946.

Segall, P. and Fitzgerald, S. (1998), A Note on Induced Stress Changes in Hydrocarbon and Geothermal Reservoirs. Tectonophysics, 289, 117-128.

Stark, M.A. (1990), Imaging Injected Water in The Geysers Reservoir Using Microearthquake Data, Geotherm. Resources Counc. Trans., 14, 1697-1704.

Stark, M.A., and Davis, S.D. (1996), Remotely Triggered Microearthquakes at The Geysers Geothermal Field, California, Geophys. Res. Lett., 23, 945-948.

Top of Layer		Vp	Vs
Depth (m)	Elevation (m)	(km/sec)	(km/sec)
0	811	3.81	1.89
244	567	3.81	2.16

Table 1. Summary of seismic velocities used.

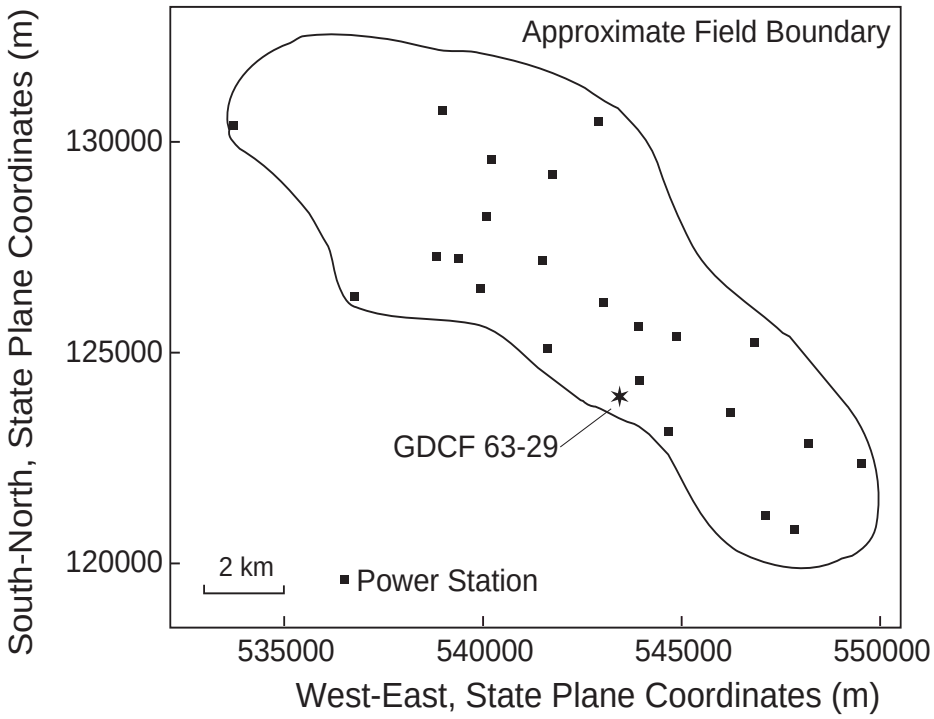

Figure 1. Location of the monitor well GDCF 63-29.

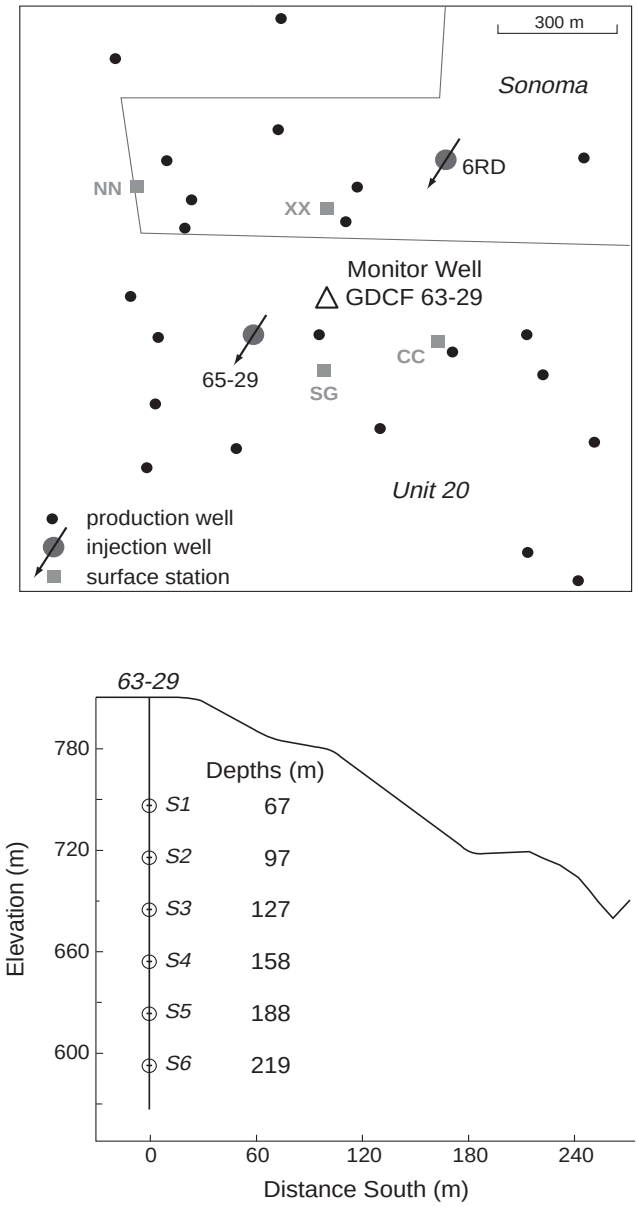

Figure 2. Map view of the monitor well GDCF 63-29, surface stations deployed to supplement the downhole array and the production and injection wells within 762 m (2500 ft) of the monitor well (top). Sonoma and Unit 20 refer to production units. Production and injection wells are mapped at their weighted midpoint of steam entries recorded while drilling. The lower diagram shows the downhole geophone configuration in GDCF-63-29. Topographic profile south of well is also shown. All depths are with respect to ground level at wellhead (811 m elevation). Station spacing is 30.48 m (100 ft).

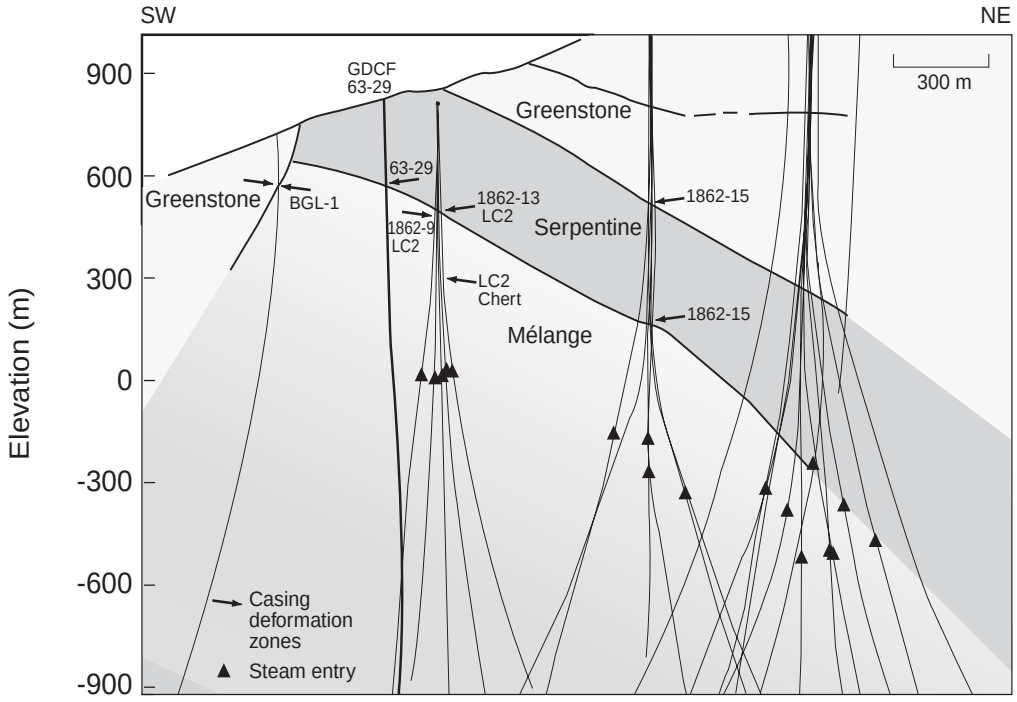

Figure 3. Geologic profile showing the well casing deformation zones association with upper and lower contacts of a serpentine unit. Profile is oriented N30E (viewing N60W). Steam entries delineate approximate top of reservoir.

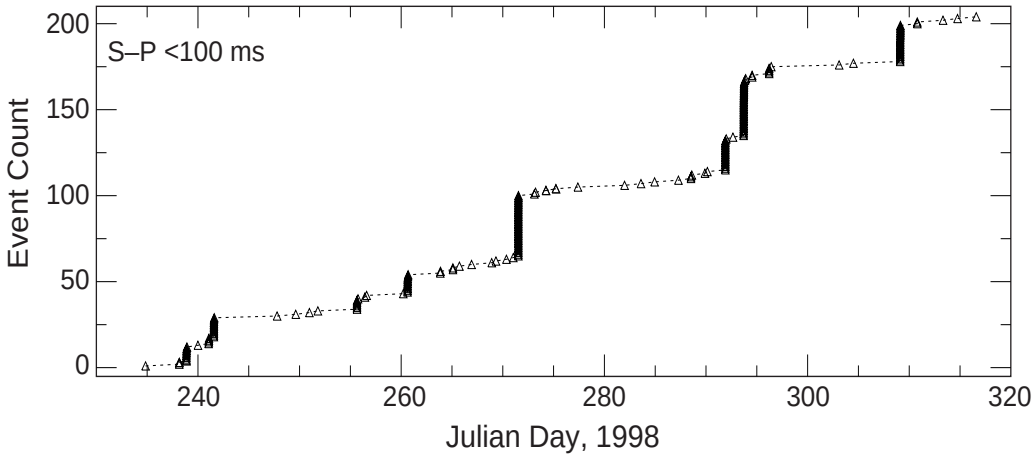

Figure 4. Cumulative event count from August 18 to November 13, 1998 for events within ~500 m of the array (S - P arrival time difference < 100 msec).

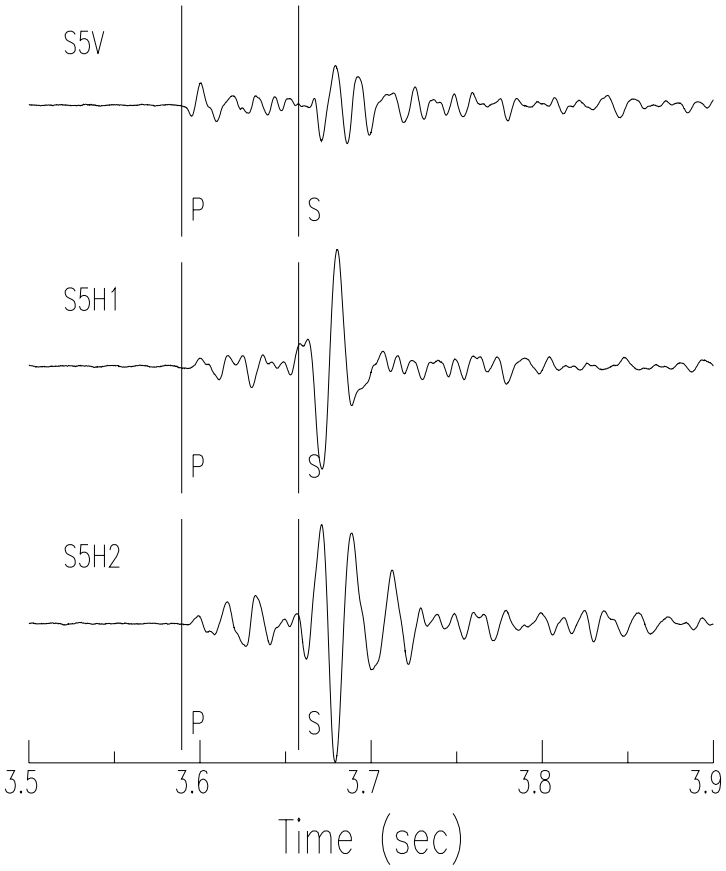

Figure 5. Example of a high-quality, shallow microearthquake recorded on downhole sonde S5.

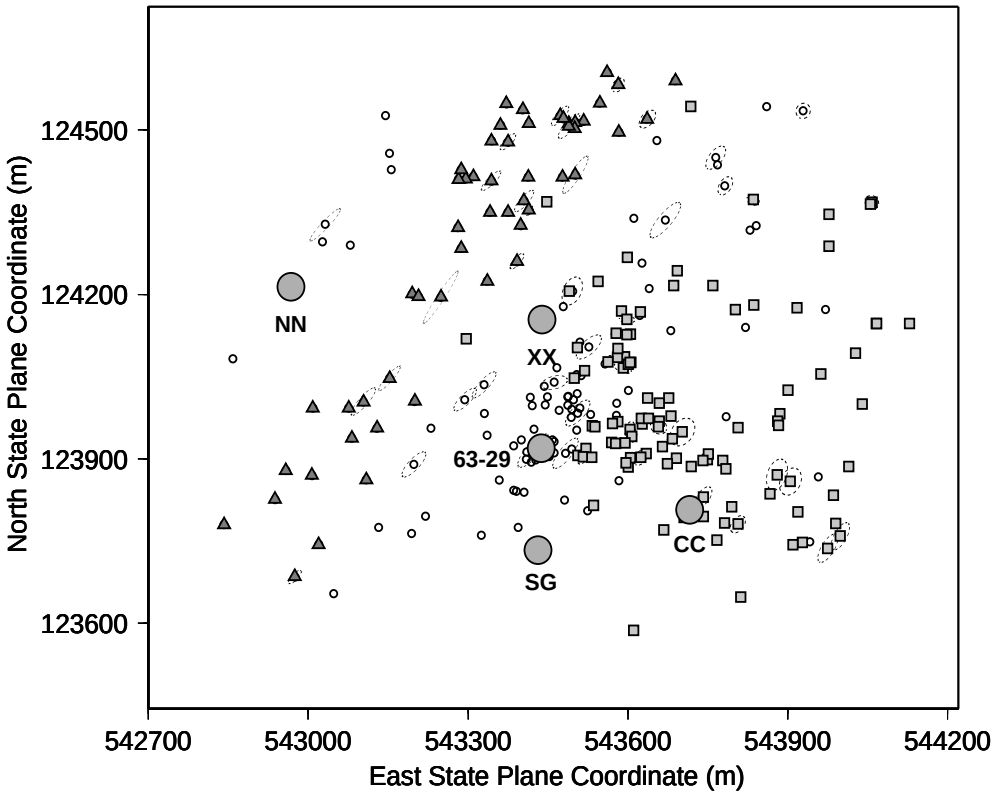

Figure 6. Map view of 248 microearthquakes detected on the downhole array in 63-29 and surrounding surface stations. The monitor well and surface stations are shown as larger shaded circles. These hypocenters had rms travel time residuals ≤ 5 msec and location errors less than 60m. Every fifth error ellipsoid projection is shown as dashed ellipses to show representative location errors. Two sub-clusters of locations are displayed as shaded square and triangle symbols and were identified based on the depth view shown in Figure 7. All other hypocenters are shown as open circles.

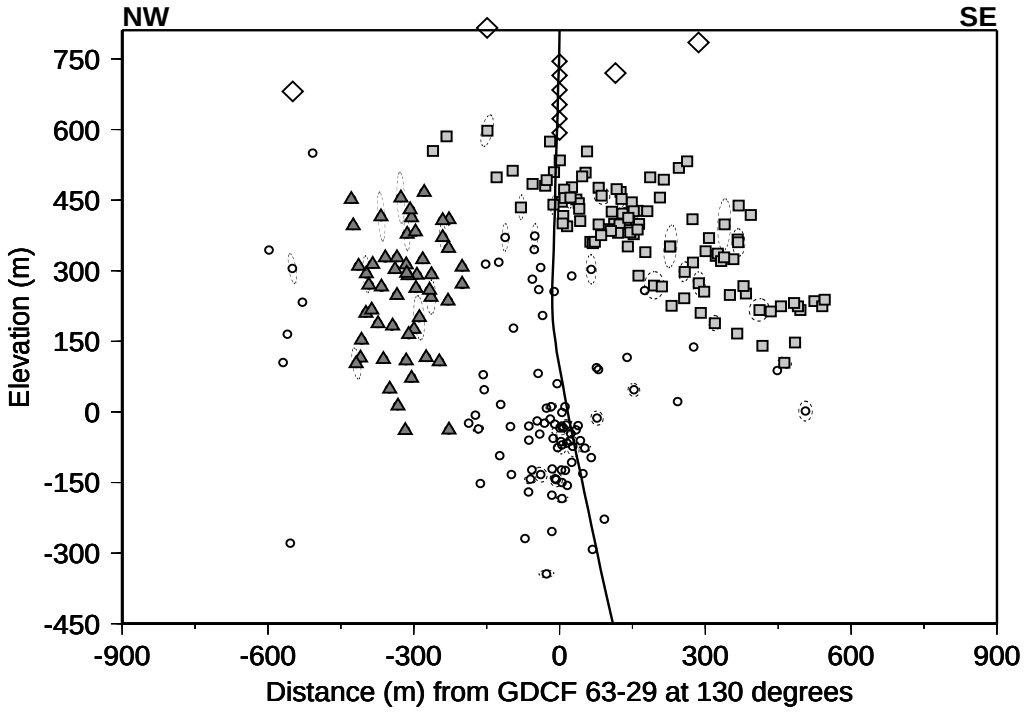

Figure 7. Depth locations of events projected onto a plane oriented 130° azimuth (viewing at N40E). Well GDCF 63-29 trace is shown. The open diamond symbols are the downhole and surface stations used. Two hypocenter groups are identified based on this projection and are distinguished by the shaded square and triangle symbols. All other hypocenters are shown as open circles. The map view of these same groups are shown in Figure 6 for a 3-dimensional visual aid. Top of reservoir is at about -180 m. Every fifth error ellipsoid projection is shown as dashed ellipses to show representative location errors.

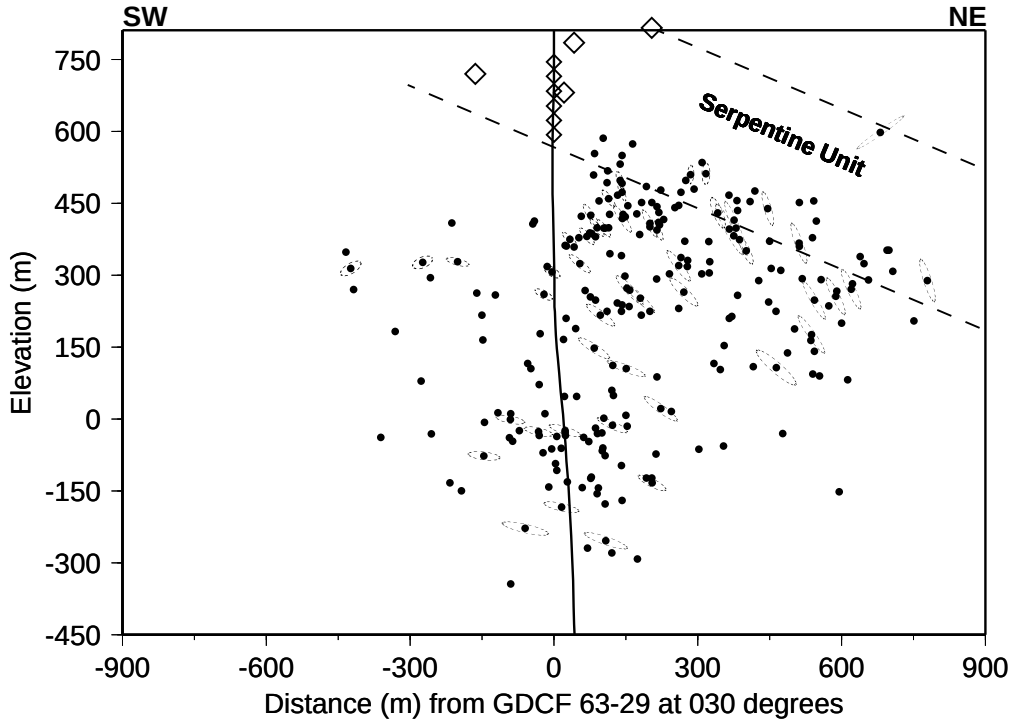

Figure 8. Depth locations of events projected onto a plane oriented N30E (viewing at N60W). Well GDCF 63-29 trace is shown. The open diamond symbols are the downhole and surface stations used. The dashed lines mark the approximate top and bottom contacts of a serpentine unit (as seen in Figure 3). Top of reservoir is at about -180 m elevation. Every fifth error ellipsoid projection is shown as dashed ellipses to show representative location errors.

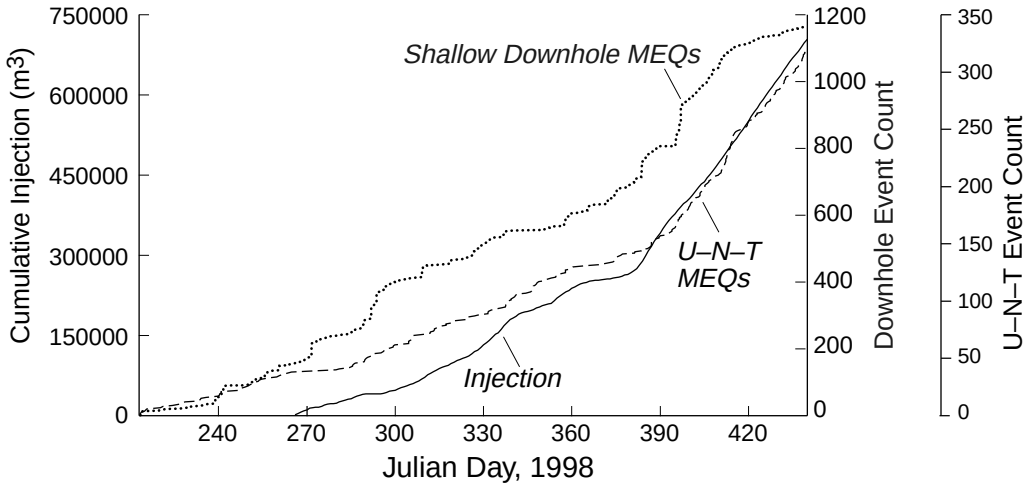

Figure 9. Cumulative injection volume in the study area and the cumulative event counts for the downhole detected events within about 750 m of the array and the U-N-T surface-array events with epicenters within 750 m of the monitor-well wellhead. Figure 2 shows the injection wells and the common epicenter area. Figure 10 shows the depth distribution of the two distinct populations of events; the downhole events consider for analysis (S - P arrival time ≤ 150 msec) occur predominantly within the overburden, whereas the larger, wider-distributed surface array detects the deeper, higher-energy reservoir events. Injection in the area was ongoing prior to day 266, but complete records were not available. Both the reservoir and overburden microseismicity increase within about one week of the increased injection rate at day 380.

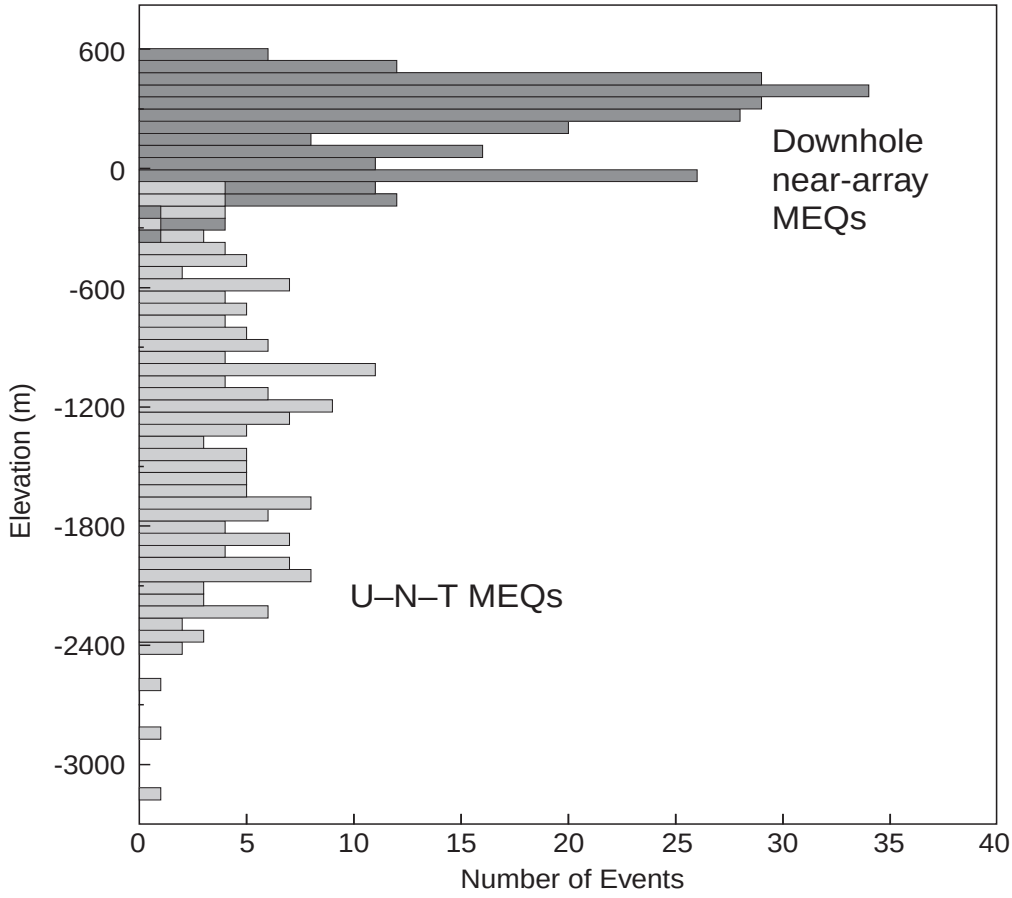

Figure 10. Depth distribution of microearthquakes detected on the U-N-T surface array at The Geysers and the shallow, downhole array in well 63-29. These are events with epicenters within the map area of Figure 2, over the common time interval January 6 to March 16, 1999. The near-array events consider for analysis from the downhole array (S - P arrival time ≤ 150 msec) are predominantly within the overburden, whereas the larger, wider-distributed surface array detects only the deeper, higher-energy reservoir events. Top of reservoir for this area is at about -180 m elevation.

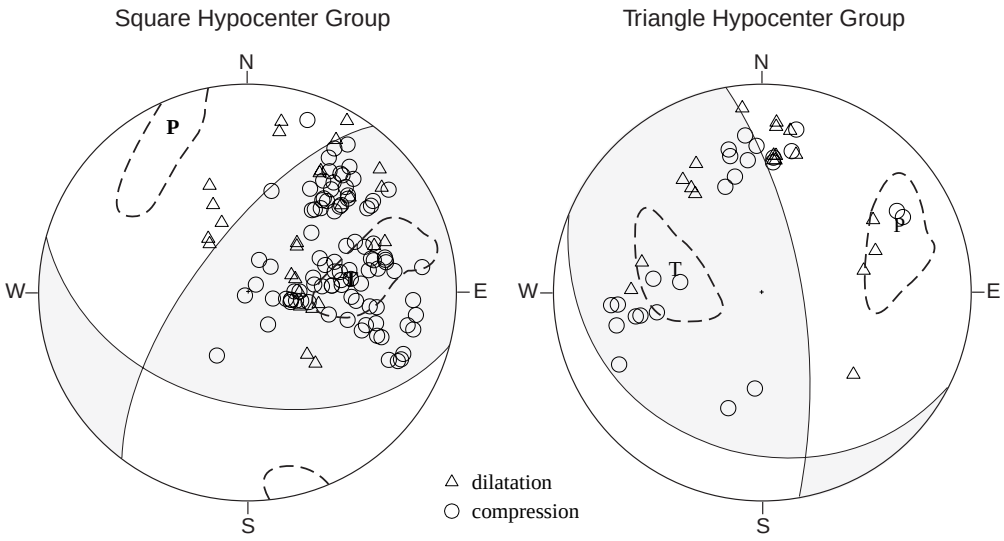

Figure 11. Composite fault-plane solutions as equal-area, lower-hemisphere projections for square- and triangle-symbol hypocenter groups shown in Figures 6 and 7. Compressive quadrants are shaded. Dashed boundaries around P and T axes show the uncertainty within the 90% confidence limit. Only first-motion data with signal-to-noise ratios ≥ 10 were used. The square-group solution has 112 first-motion data with 15% discrepant; the triangle-group solution has 43 first-motion data with 28% discrepant.